TECHNISCHE UNIVERSITÄT DRESDEN

Fakultät Umweltwissenschaften

Hydro-Mechanical-Chemical Coupled Processes in Fractured Porous Media: Pressure Solution Creep

Dissertation for awarding the academic degree Doctor of Engineering (Dr.-Ing)

Submitted by

M.Sc. Renchao Lu

21/10/1988 in P.R. China

Supervisor:

Prof. Dr. -Ing. Olaf Kolditz,

Technische Universität Dresden.

Jun.-Prof. Dr. rer. nat. Haibing Shao,

Technische Universität Bergakademie Freiberg.

Date of the oral defence: 22.11.2019

Leipzig, October 2018

Erklärung zur Eröffnung des Promotionsverfahrens:

1. Hiermit versichere ich, dass ich die vorliegende Arbeit ohne unzulässige Hilfe Dritter und ohne Benutzung anderer als der angegebenen Hilfsmittel angefertigt habe; die aus fremden Quellen direkt oder indirekt übernommenen Gedanken sind als diese kenntlich gemacht.

2. Bei der Auswahl und Auswertung des Materials sowie bei der Herstellung des Manuskriptes habe ich Unterstützungsleistungen von folgenden Personen erhalten:

   Jun.-Prof. Dr. rer. nat. Haibing Shao, Dr. -Ing. Norihiro Watanabe,
   Prof. Dr. Thomas Nagel
   .....

3. Weitere Personen waren an der geistigen Herstellung der vorliegenden Arbeit nicht beteiligt. Insbesondere habe ich nicht die Hilfe eines kommerziellen Promotionsberaters in Anspruch genommen. Dritte haben von mir weder unmittelbar noch mittelbar geldwerte Leistungen für Arbeiten erhalten, die im Zusammenhang mit dem Inhalt der vorgelegten Dissertation stehen.

4. Die Arbeit wurde bisher weder im Inland noch im Ausland in gleicher oder ähnlicher Form einer anderen Prüfungsbehörde vorgelegt und ist – sofern es sich nicht um eine kumulative Dissertation handelt – auch noch nicht veröffentlich worden.

5. Sofern es sich um eine kumulative Dissertation gemäß § 10 Abs. 2 handelt, versichere ich die Einhaltung der dort genannten Bedingungen.

6. Ich bestätige, dass ich die Promotionsordnung der Fakultät Umweltwissenschaften der Technischen Universität Dresden anerkenne.

Leipzig, 10. Okt. 2018

Ort, Datum

Unterschrift des Doktoranden

ÜBEREINSTIMMUNGSERKLÄRUNG

Die Übereinstimmung dieses Exemplars mit dem Original der Dissertation zum Thema:

'Hydro-Mechanical-Chemical Coupled Processes in Fractured Porous Media: Pressure Solution Creeep'

wird hiermit bestätigt.

.....
Ort, Datum

.....
Unterschrift (Vorname Name)

ABSTRACT

Pressure solution creep is a fundamental deformation mechanism in the upper crust. Overburden pressure that acts upon layers of sediment leaves grains densely packed. Nonhydrostatic stress distributed over the contacts between grains brings an enhancement effect on surface dissolution. As surface retreat over the contacts and hence grain repacking squeeze out pore water in the voids, the layers of sediment are deformed to become denser and denser.

This work aims to identify what process slows down pressure solution creep over time. For this purpose, a new mechanistic model of pressure solution creep is developed, derived from the reaction rate law for nonhydrostatic dissolution kinetics under the hypothesis of a closed system. The present mechanistic model shows that (1) the creep rate goes down as a combined consequence of stress transfer across expanding contacts and concentration build-up in the interlayer of absorbed water; and (2) solute migration process acts as the primary rate-limiting process of pressure solution creep in the long run.

This work then focuses on hydraulic evolution of channelling flow through a single deformable fracture which is simultaneously subjected to pressure solution creep. The developed 1-D reactive transport model is allowed to capture the strong interaction between channelling flow and pressure solution creep under crustal conditions. This numerical investigation provides a justified interpretation for the unusual experimental observation that fracture permeability reduction does not necessarily cause concentration enrichment. Temperature elevation contributes to accelerating the progression of pressure solution creep.

ZUSAMMENFASSUNG

Drucklösungskriechen ist ein grundlegender Verformungsmechanismus in der oberen Kruste. Der übermäßige Druck, der auf Sedimentschichten wirkt, hinterlässt die Körner dicht gepackt. Nichthydrostatische Spannung, die über die Kontakte zwischen den Körnern verteilt ist, bewirkt eine Verbesserung der Oberflächenauflösung. Wenn sich die Oberfläche über die Kontakte zurückzieht und das Korn erneut verpackt wird, drückt es Porenwasser in den Hohlräumen aus, und die Sedimentschichten werden so verformt, dass sie dichter und dichter werden.

Diese Arbeit zielt darauf ab, zu ermitteln, welcher Prozess das Kriechen der Drucklösung mit der Zeit verlangsamt. Zu diesem Zweck wird ein neues mechanistisches Modell des Drucklösungskriechens entwickelt, das aus dem Reaktionsgeschwindigkeitsgesetz für die nichthydrostatische Auflösungskinetik unter der Hypothese eines geschlossenen Systems abgeleitet wird. Das vorliegende mechanistische Modell zeigt, dass (1) die Kriechgeschwindigkeit als kombinierte Folge von Spannungsübertragung über sich ausdehnende Kontakte und Konzentrationsaufbau in der Zwischenschicht aus absorbiertem Wasser abnimmt; und (2) der Migrationsprozess des gelösten Stoffes wirkt auf lange Sicht als primärer geschwindigkeitsbegrenzender Prozess des Drucklösungskriechens.

Diese Arbeit konzentriert sich dann auf die hydraulische Entwicklung des Kanalflusses durch eine einzelne verformbare Bruchstelle, die gleichzeitig einem Drucklösungskriechen ausgesetzt ist. Das entwickelte 1-D reaktive Transportmodell kann die starke Wechselwirkung zwischen dem Kanalfluss und dem Kriechen der Drucklösung unter Krustenbedingungen erfassen. Diese numerische Untersuchung liefert eine begründete Interpretation für die ungewöhnliche experimentelle Beobachtung, dass die Verringerung der Bruchpermeabilität nicht notwendigerweise eine Konzentrationsanreicherung verursacht. Die Temperaturerhöhung trägt dazu bei, das Fortschreiten der Drucklösung zu beschleunigen.

ACKNOWLEDGEMENTS

I would like to express my sincere gratitude to Dr. Wenqing Wang who recommended me to Prof. Dr. Olaf Kolditz, and gave me many technical instructions in numerical methods.

I wish to express the deepest sense of gratitude to my supervisor Prof. Dr. Olaf Kolditz who brought me to the department of environmental informatics, Helmholtz Centre of Environmental Research - UFZ where I started up a new chapter of my life, and offered me advise, support, and encouragement throughout my PhD study. So fortune to work in his department. The four-year study abroad experience is memorable and is a good fortune for my academic career and personal life.

I owe sincere gratitude to my cosupervisor Jun.-Prof. Dr. Haibing Shao for his continuous supervision, unwavering support, and considerable contribution of time throughout my study. I appreciate his mentorship.

I am very grateful to Dr. Norihiro Watanabe and Prof. Thomas Nagel who are supportive, dedicated, and always encourage me to think critically and creatively. Without their help, I cannot grow as an independent scholar.

This work would not have been finished without the robust OpenGeoSys platform, so I want to thank the developer team for their long-term efforts and great contribution.

I feel indebted to all the department colleagues who have provided me with their unconditional support. I would like to take this opportunity to express my deep gratitude.

Furthermore, I would like to acknowledge China Scholarship Council whose financial support allows me to focus on the research work presented in the dissertation.

Most of all, I want to thank my parents for upbringing and education. Special thanks and appreciation go to my wife Qing Zou for her love, inspiration, support, and accompany.

CONTENTS

I BACKGROUND

1 INTRODUCTION 2
- 1.1 Motivations 2
- 1.2 Challenges and state of the art 3
- 1.3 Scope of this thesis 4
- 1.4 Outline of this thesis 4

II THEORY

2 STRESS-INDUCED DISSOLUTION ENHANCEMENT 7

3 ATTENUATION CHARACTERISTIC OF PRESSURE SOLUTION 9

4 FORMULATION OF CLOSURE CHARACTERISTIC RELATIONSHIP 11
- 4.1 Basic concepts 11
- 4.2 Pore volume reduction 11
- 4.3 Contact area expansion 12

5 REACTIVE SOLUTE TRANSPORT IN FRACTURES 16
- 5.1 Channelling flow 16
- 5.2 Reactive solute transport 16
- 5.3 Hydraulic feedback on surface dissolution 18

III SIMULATION

6 MODELING 22
- 6.1 Problem description 22
- 6.2 Model setup 22

7 RESULTS AND DISCUSSION 27
- 7.1 Comparison against laboratory experiments 27
- 7.2 Insights into fracture permeability evolution 27
- 7.3 Insights into element concentration evolutions 28
- 7.4 Comparison against existing relations 30
- 7.5 Impact of fracture channel topography 30

IV SUMMARY

8 CONCLUSIONS AND OUTLOOK 34

V APPENDIX

9 APPENDIX 36
- 9.1 Geometry factors 36
- 9.2 Publications 38

Part I

BACKGROUND

1

INTRODUCTION

1.1 MOTIVATIONS

Public concerns about global warming, radioactive waste safety, and fast-growing demands for clean renewable energy prosper subsurface engineered applications worldwide, such as geological carbon sequestration, nuclear waste disposal, and deep geothermal reservoirs. In this context, problem-oriented field-scale multiphysics simulation in coordination with specific laboratory-scale experiments is regarded as an effective means of achieving scientific decision-making in site selection and making proper assessment in storage capacity, sustainability, and safety. Mechanistic model development in terms of the process of major concern is thus placed uppermost in performing field-scale multiphysics simulation.

This contribution focuses on pressure solution creep which is active throughout the lifespan of geological applications as a fundamental deformation mechanism in the upper crust. Pressure solution creep, in terms of terminology, is the term that describes a microscopic deformation mechanism by nonhydrostatic dissolution over the contacts between densely packed grains. The open status of the subsystem where nonhydrostatic dissolution takes place conditions that the dissolution process is not standalone, followed by diffusive transport into the pores outside the contacts. Concentration enrichment and hence probable solute supersaturation may further cause secondary precipitates to be formed and cemented around the contacts over geological time scales.

Developing a mechanistic model, in terms of pressure solution creep, has far-reaching implications for diagnesis of sedimentary basins in the early age (Tada and Siever, 1989), interseimic healing and sealing of fault gouge (Evans and Chester, 1995), as well as reactive solute transport in densely packed granular geomaterials. Based upon the desired mechanistic model, field-scale multiphysics simulation would be a more powerful scientific tool for assessing the long-term storage capacity of carbon dioxide in a target stratum, barrier effect of bentonite to escaped radionuclides, and efficiency of geothermal exploitation during designed operation period (Taron and Elsworth, 2009).

1.2 CHALLENGES AND STATE OF THE ART

Pressure solution creep has been moderately understood in the past decades (Weyl, 1959; Paterson, 1973; De Boer, 1977; Rutter, 1983; Heidug, 1995; Lehner, 1995; Revil, 1999; Bos and Spiers, 2002; Yasuhara, Hideaki and Elsworth, Derek and Polak, Amir, 2004; Taron, Joshua and Elsworth, Derek, 2010; Neretnieks, 2014; Bernabé and Evans, 2014; Lang et al., 2015; Lu et al., 2018), for one of the two most significant concerns has been addressed — how does nonhydrostatic stress arouse dissolution enhancement. The classical thermodynamic model developed by Weyl (1959), Paterson (1973), De Boer (1977), Rutter (1983), and Heidug (1995) has established and accounted for the association between nonhydrostatic stress and dissolution enhancement. The other concern remains yet unresolved as to what process slows down pressure solution creep over time. There is a common recognition that the creep rate goes down as a consequence of contact area expansion. Stress transfer across expanding contacts reduces the enhancement effect on surface dissolution. If that is the case, pressure solution creep would not cease to the end as observed in the flow-through experiments (Moore et al., 1994; Polak et al., 2003; Polak et al., 2004; Yasuhara et al., 2006; Yasuhara et al., 2011). It turns out that an additional process gets involved, thereby leading to the ceasing of pressure solution creep. Thus, it does make sense to figure out what process acts as the rate-limiting process of pressure solution creep in the long run.

In effect, pressure solution creep makes pore volume reduction and contact area expansion with the mass removal from contacts. As the volumetric reduction shows apparently higher relevance to the evolution of hydraulic properties which is one of the most concerns (e.g., porosity with respect to granular matter and permeability to fractures), the focus on pore volume reduction naturally outweighs on contact area expansion so that the interaction between contact area expansion and pressure solution creep has not gained much attention either. In fact, such an overlooked interaction impacts and runs throughout pressure solution creep process. Contact area expansion brings out an attenuation effect on the surface dissolution via stress transfer across expanding contacts, and in the meanwhile, intervenes the follow-up solute migration process by lengthening the solute diffusion route. Since the solute migration process is being regarded not as the primary rate-limiting process of pressure solution creep, the first contribution of contact area expansion is assigned a relatively higher priority than the second in investigation. Nevertheless, to the authors' knowledge, none other than Yasuhara, Hideaki and Elsworth, Derek and Polak, Amir (2004) and Lang et al. (2015) have made commitments to the first contribution. The commitments to the second one are even less. Yasuhara, Hideaki and Elsworth, Derek and Polak, Amir (2004) proposed a phenomenological law for characterizing attenuation of dissolution enhancement at contacts. With successful applications of the phenomenological law in reproducing typical flow-through experiments (Yasuhara et al., 2006; Yasuhara et al., 2011; Ogata et al., 2018), the interaction

between contact area expansion and pressure solution creep regains focus and is confirmed as the key to understand fracture permeability evolution under hydrothermal conditions. On the other hand, the weakness of the phenomenological law is rather apparent, most notably in loosely binding with the target physical process - the extreme extent of contact area expansion in reach of chemical compaction equilibrium is estimated from the latent heat of fusion (Stephenson et al., 1992; Revil, 1999). Lang et al. (2015) further tuned the phenomenological law where the complementary constraint on the contact area ratio is relieved. To more accurately and inherently describe the interaction between contact area expansion and pressure solution creep, we are motivated to formulate a closure characteristic relationship which is compatible with the new thermodynamic model.

To further consolidate the closure characteristic relationship once completed, a well-designed demonstration experiment is desirable. Differing from the conventional flow-through experiments which are designed for investigating hydraulic feedback on pressure solution creep under varying hydrothermal conditions (e.g., temperature (Polak et al., 2003), confining stress (Zhang et al., 2010), differential hydraulic pressure / volumetric flow rate (Yasuhara et al., 2006), and fluid chemistry (Zhang and Spiers, 2005)), the desired demonstration experiment aims at (1) measuring to what extent contact area expansion will cease in the context of pressure solution creep; (2) examining the reliability of the proposed closure characteristic relationship; and (3) identifying the primary rate-limiting process in pressure solution creep. So far no experiment of this type has been reported yet.

1.3 SCOPE OF THIS THESIS

This contribution concerns formulation of a new mechanistic model of pressure solution creep. As an essential supplement to the above mechanistic model, the demonstration experiment in demand is now ongoing but not about to be presented herein as part of the thesis. Following on the mechanistic model development, a more advanced reactive transport model is developed to investigate hydro-chemical coupled problems in deformable fractures in the context of pressure solution creep under crustal conditions. This numerical investigation, on the one hand, aims at examining the exact performance of the kernel mechanistic model in a real scenario. On the other hand, we expect to accurately capture both hydraulic and concentration features observed in the experimental work of Yasuhara et al. (2011) by our present model and to physically account for these highlighted features.

1.4 OUTLINE OF THIS THESIS

This thesis is structured as follows. Chapter 2 focuses on stress-induced dissolution enhancement. Chapter 3 highlights attenuation characteristic of

pressure solution. Chapter 4 is on the formulation of the new mechanistic model of pressure solution creep. Chapter 5 presents a complete theoretical framework for addressing hydro-chemical coupled problems in deformable fractures. Chapter 6 details numerical implementation for modeling channelling flow and reactive solute transport. Chapter 7 provides insights into hydraulic and concentration features in response to pressure solution creep.

Part II

THEORY

2

STRESS-INDUCED DISSOLUTION ENHANCEMENT

Nonhydrostatic stress distributed over the contacts between grains causes chemical potential of the dissolving solid to increase. As a result, the chemical potential of the solid phase under loading condition takes the form

$$\mu_{\mathrm{s}}\left(\sigma_{\mathrm{n}}, T\right) = f_{\mathrm{s}}\left(\sigma_{\mathrm{n}}, T\right) + \sigma_{\mathrm{n}} V_{\mathrm{m}} - 2H\gamma_{\mathrm{G}}, \tag{2.1}$$

while the counterpart at elsewhere in the situation of hydrostatic pressure has

$$\mu_{\mathrm{s}}\left(p_{\mathrm{w}}, T\right) = f_{\mathrm{s}}\left(p_{\mathrm{w}}, T\right) + p_{\mathrm{w}} V_{\mathrm{m}}, \tag{2.2}$$

where σ_{n} [Pa] is the normal contact stress, p_{w} [Pa] is the hydrostatic pressure, T [K] is the absolute temperature, f_{s} [J/mol] is the molar Helmholtz free energy dependent on nonhydrostatic stress / hydrostatic pressure and temperature, V_{m} [m^3/mol] is the molar volume, H [-] is the interface curvature, and γ_{G} [J/mol] is the molar Gibbs surface energy.

The stress-induced difference in the chemical potential of the solid phase between the contacts and free-face grain surfaces is then given by subtracting equation (2.2) from equation (2.1)

$$\Delta\mu_{\mathrm{s}} = \mu_{\mathrm{s}}\left(\sigma_{\mathrm{n}}, T\right) - \mu_{\mathrm{s}}\left(p_{\mathrm{w}}, T\right), \tag{2.3}$$

i.e.,

$$\Delta\mu_{\mathrm{s}} = \Delta f_{\mathrm{s}} + \left(\sigma_{\mathrm{n}} - p_{\mathrm{w}}\right) V_{\mathrm{m}} - 2H\gamma_{\mathrm{G}}, \tag{2.4}$$

where Δf_{s} [J/mol] is the molar Helmholtz free energy difference.

By utilizing the relation between the chemical potential and activity

$$\mu\left(p, T\right) = \mu^{*} + RT\ln a, \tag{2.5}$$

the activity of the solid phase under nonhydrostatic stress condition is presented by reference to the situation of hydrostatic pressure

$$a_{\mathrm{s}}^{\sigma} = a_{\mathrm{s}}^{p}\exp\left(\frac{\Delta\mu_{\mathrm{s}}}{RT}\right) \approx a_{\mathrm{s}}^{p}\exp\left[\frac{\left(\sigma_{\mathrm{n}} - p_{\mathrm{w}}\right) V_{\mathrm{m}}}{RT}\right], \tag{2.6}$$

where μ^{*} [J/mol] is the chemical potential of the solid / liquid phase under a set of standard conditions (p, T), and a_{s}^{p} [-] is the activity of the solid phase under hydrostatic pressure. For the sake of simplicity, the terms for Helmholtz free energy difference and Gibbs surface energy are neglected.

The normal contact stress is normally linked with the macroscopic confining stress σ_{con} which is imposed on the bisected dense rock mass as

$$\sigma_{\mathrm{n}} = \frac{\sigma_{\mathrm{eff}}}{R_{\mathrm{c}}} = \frac{\sigma_{\mathrm{con}} - p_{\mathrm{w}}}{R_{\mathrm{c}}}, \tag{2.7}$$

where σ_{eff} [Pa] is the effective stress, and R_{c} [-] is the contact area ratio.

Dissolution kinetics under whatever conditions, in principle, depends upon the chemical potential difference between the solid and liquid phase in a system. Equation (2.6) shows that dissolution enhancement under loading condition is due to the increase of the chemical potential of the solid phase from the external work done by the nonhydrostatic stress.

To the knowledge of the presented classical thermodynamic model, the enhancement effect on the surface dissolution will not vanish unless the state of stress is fundamentally changed.

3

ATTENUATION CHARACTERISTIC OF PRESSURE SOLUTION

Pressure solution presents attenuation characteristic as free-face dissolution does, specifically shown in the decrease of the rate of the mass removal from contacts over time. In the context of pressure solution, the normalized mass removal rate $\dot{m}$ [mol/m^2/s] follows a more general reaction rate law where the activity of the dissolving solid is no longer implicit (Palandri and Kharaka, 2004; Taron, Joshua and Elsworth, Derek, 2010)

$$\dot{m}^{\mathrm{c}} = \sum_{n} k_n^{+} a_{\mathrm{s}}^{\sigma} \left(1 - \frac{Q}{a_{\mathrm{s}}^{\sigma} K_{\mathrm{eq}}}\right), \quad n = \text{acid, neutral, and base,} \tag{3.1}$$

where k^{+} [mol/m^2/s] and K_{eq} [-] are the dissolution rate constant and equilibrium constant at hydrostatic pressure and ambient temperature, and Q [-] is the ion activity product representing the chemical potential of the liquid phase.

The dissolution rate constant is calculated from the Arrhenius equation (Palandri and Kharaka, 2004)

$$k^{+} = A\, e^{E/RT}\, a_{\mathrm{H}^{+}}^{n_{\mathrm{H}^{+}}}, \tag{3.2}$$

where A [mol/m^2/s] is the pre-exponential factor, E [J/mol] is the activation energy, $a_{\mathrm{H}^{+}}$ is the activity of the hydrogen ion, and $n_{\mathrm{H}^{+}}$ is the H^{+} catalysis constant.

Attenuation characteristic arises from the decrease of the chemical potential difference between the solid and liquid phase in the system. The reaction rate law for pressure solution kinetics shows that decrease of the chemical potential difference is a combined consequence of stress transfer across expanding contacts and concentration build-up in the interlayer of absorbed water. However, concentration build-up in the interlayer is being regarded not as a primary rate-limiting process as stress transfer across expanding contacts, because the concentration gradient between inside and outside is thought steep throughout pressure solution process such that few of solutes would remain in the interlayer under the overwhelming driving force. Solutes mostly escape from the open system, migrating into the pores outside the contacts. That may be not the case. As pressure solution creep proceeds, stress transfer across expanding contacts, lengthening of the solute diffusion

route, and concentration enrichment in the pore cause the concentration gradient to decrease. More and more solutes are consequently constrained in the interlayer.

4

FORMULATION OF CLOSURE CHARACTERISTIC RELATIONSHIP

4.1 BASIC CONCEPTS

This chapter starts by introducing a number of geometrical quantities for describing a representative elementary volume where two identical grains are in contact under loading and draining conditions.

The contact area ratio R_c [-] is a measure of total contact area A^c [m^2] over representative elementary area A^t [m^2]

$$R_c = \frac{A^c}{A^t}. \tag{4.1}$$

Elsewhere pertains to free-face grain surfaces A^p [m^2].

The geometric aperture b [m] is a measure of opening of intergrain voids which becomes zero within the contacts and positive out of the contacts. The mean aperture b_m [m] is a frequently used statistical parameter, defined as

$$b_m = \frac{1}{A^t} \int_{A^t} b \, dA. \tag{4.2}$$

As geofluid passes around contacts in channelling flow, statistics of non-zero geometric apertures may make more sense to hydraulics. Thus, another representative area-averaged quantity referred as averaged non-zero aperture b_m^p [m] comes out with the definition of

$$b_m^p = \frac{1}{A^p} \int_{A^p} b \, dA. \tag{4.3}$$

Note that the two representative geometrical quantities b_m and b_m^p can be interconverted by

$$b_m = (1 - R_c) \cdot b_m^p. \tag{4.4}$$

4.2 PORE VOLUME REDUCTION

Surface retreat over asperity contacts often leads to pore volume reduction and contact area expansion which can be properly parametrized by b_m^p and R_c.

Given contact area expansion, the surface retreat in amount is not absolutely equal to the averaged change of non-zero geometric apertures. For the sake of simplicity, we assume the equality still holds

$$\frac{1}{2}\,\dot{b}_{\mathrm{m}}^{\mathrm{pc}} = -\,V_{\mathrm{m}}\,\dot{m}^{\mathrm{c}}. \tag{4.5}$$

Adding more superscripts to $\dot{b}_{\mathrm{m}}^{\mathrm{p}}$ expects to exactly show what makes pore volume reduction. The product of molar volume V_{m} and normalized mass removal rate $\dot{m}^{\mathrm{c}}$ represents the average vertical retreat rate over the contacts.

4.3 CONTACT AREA EXPANSION

Contact area expansion can be precisely tracked on closure characteristic curves where averaged non-zero mechanical aperture $b_{\mathrm{m}}^{\mathrm{p}}$ and contact area ratio R_{c} serve as the representative parameters. The closure characteristic curves are ideally presented in form of scatter plot, converted from available aperture distribution histograms. For most cases, aperture distribution histograms are beyond the reach of model developers, yet there still remains a chance to access the desired closure characteristic curves.

Methodologically, we first prototype the real-world flow channel by generating a reference closure characteristic curve from concerned physical process. The generated reference closure characteristic curve is then calibrated toward the target configuration. The following will go into detail about how to perform the process-based generation approach proposed herein to reproduce the authentic closure characteristic relationship.

Substituting equations (2.6), (2.7), and (3.1) into equation (4.5) yields

$$\frac{1}{2}\,\dot{b}_{\mathrm{m}}^{\mathrm{pc}} = \underbrace{-V_{\mathrm{m}}\sum_{n} k_n^{+}\,a_{\mathrm{s}}^{p}\exp\left[\frac{V_{\mathrm{m}}}{RT}\left(\frac{\sigma_{\mathrm{eff}}}{R_{\mathrm{c}}}-p_{\mathrm{w}}\right)\right]}_{F(t)\cdot G(R_{\mathrm{c}})\,=\,F(t)\cdot G(R_{\mathrm{c}}(b_{\mathrm{m}}^{\mathrm{p}}))} + \underbrace{V_{\mathrm{m}}\sum_{n} k_n^{+}\frac{Q}{K_{\mathrm{eq}}}}_{P(t)}. \tag{4.6}$$

The right-hand-side terms are split into two groups, i.e., one term depending on R_{c} and one another which does not. The former can be abstracted as the product of a time-dependent function $F(t)$ and a function of contact area ratio $G(R_{\mathrm{c}})$, while the latter constitutes another time-dependent function $P(t)$. The function $G(R_{\mathrm{c}})$ can be further understood as a function of averaged non-zero aperture $G(R_{\mathrm{c}}(b_{\mathrm{m}}^{\mathrm{p}}))$.

Functional abstraction of the right-hand-side terms unveils equation (4.6) in standard form of first-order non-homogeneous differential equation. The homogeneous part of the equation is readily solved

$$\frac{1}{2}\,\dot{b}_{\mathrm{m}}^{\mathrm{pc}} = -V_{\mathrm{m}}\sum_{n} k_n^{+}\,a_{\mathrm{s}}^{p}\exp\left[\frac{V_{\mathrm{m}}}{RT}\left(\frac{\sigma_{\mathrm{eff}}}{R_{\mathrm{c}}}-p_{\mathrm{w}}\right)\right]. \tag{4.7}$$

Rearranging equation (4.7) and integrating on both sides produces

$$\frac{1}{2}\int_{b^{\mathrm{p}}_{\mathrm{m0}}}^{b^{\mathrm{p}}_{\mathrm{m}}} \exp\left[-\frac{V_{\mathrm{m}}}{RT}\left(\frac{\sigma_{\mathrm{eff}}}{R_{\mathrm{c}}}-p_{\mathrm{w}}\right)\right]\mathrm{d}b^{\mathrm{p}}_{\mathrm{m}} = \int_0^t -V_{\mathrm{m}}\sum_n k_n^+ a_{\mathrm{s}}^p\,\mathrm{d}t + c, \tag{4.8}$$

where c [m] is a constant.

We then assume that contact area expansion solely takes place around the pre-existing contacts. Those independent contacts probably formed in aperture closure are neglected, otherwise the continuity of the variable R_{c} cannot be assured. Applying integration by parts to the left-hand-side term under the assumption of continuity, we have

$$\begin{aligned}&\frac{1}{2}b^{\mathrm{p}}_{\mathrm{m}}\exp\left[-\frac{V_{\mathrm{m}}}{RT}\left(\frac{\sigma_{\mathrm{eff}}}{R_{\mathrm{c}}^{\mathrm{ref}}}-p_{\mathrm{w}}\right)\right]-\frac{1}{2}b^{\mathrm{p}}_{\mathrm{m0}}\exp\left[-\frac{V_{\mathrm{m}}}{RT}\left(\frac{\sigma_{\mathrm{eff}}}{R_{\mathrm{c0}}}-p_{\mathrm{w}}\right)\right]\\&-\frac{1}{2}\int_{R_{\mathrm{c0}}}^{R_{\mathrm{c}}^{\mathrm{ref}}} b^{\mathrm{p}}_{\mathrm{m}}\exp\left[-\frac{V_{\mathrm{m}}}{RT}\left(\frac{\sigma_{\mathrm{eff}}}{R_{\mathrm{c}}}-p_{\mathrm{w}}\right)\right]\frac{\sigma_{\mathrm{eff}}V_{\mathrm{m}}}{R_{\mathrm{c}}^2RT}\,\mathrm{d}R_{\mathrm{c}} = \int_0^t -V_{\mathrm{m}}\sum_n k_n^+ a_{\mathrm{s}}^p\,\mathrm{d}t + c,\end{aligned} \tag{4.9}$$

where $R_{\mathrm{c}}^{\mathrm{ref}}$ is the property of the prototyped flow channel.

Setting c as a time-dependent function $c(t)$ and substituting equation (4.9) into equation (4.6), we obtain the particular solution of the non-homogeneous differential equation

$$c(t) = \int_0^t V_{\mathrm{m}}\sum_n k_n^+\exp\left[-\frac{V_{\mathrm{m}}}{RT}\left(\frac{\sigma_{\mathrm{eff}}}{R_{\mathrm{c}}}-p_{\mathrm{w}}\right)\right]\frac{Q}{K_{\mathrm{eq}}}\mathrm{d}t. \tag{4.10}$$

The complete solution of the first-order non-homogeneous differential equation comes out

$$\begin{aligned}&\frac{1}{2}b^{\mathrm{p}}_{\mathrm{m}}\exp\left[-\frac{V_{\mathrm{m}}}{RT}\left(\frac{\sigma_{\mathrm{eff}}}{R_{\mathrm{c}}^{\mathrm{ref}}}-p_{\mathrm{w}}\right)\right] = \frac{1}{2}b^{\mathrm{p}}_{\mathrm{m0}}\exp\left[-\frac{V_{\mathrm{m}}}{RT}\left(\frac{\sigma_{\mathrm{eff}}}{R_{\mathrm{c0}}}-p_{\mathrm{w}}\right)\right]\\&+\frac{1}{2}\int_{R_{\mathrm{c0}}}^{R_{\mathrm{c}}^{\mathrm{ref}}} b^{\mathrm{p}}_{\mathrm{m}}\exp\left[-\frac{V_{\mathrm{m}}}{RT}\left(\frac{\sigma_{\mathrm{eff}}}{R_{\mathrm{c}}}-p_{\mathrm{w}}\right)\right]\frac{\sigma_{\mathrm{eff}}V_{\mathrm{m}}}{R_{\mathrm{c}}^2RT}\,\mathrm{d}R_{\mathrm{c}}\\&+\int_0^t\left\{-V_{\mathrm{m}}\sum_n k_n^+ a_{\mathrm{s}}^p + V_{\mathrm{m}}\sum_n k_n^+\exp\left[-\frac{V_{\mathrm{m}}}{RT}\left(\frac{\sigma_{\mathrm{eff}}}{R_{\mathrm{c}}}-p_{\mathrm{w}}\right)\right]\frac{Q}{K_{\mathrm{eq}}}\right\}\mathrm{d}t.\end{aligned} \tag{4.11}$$

According to equation (4.8), the last integral term on the right-hand side can be substituted by

$$\begin{aligned}&\int_0^t\left\{-V_{\mathrm{m}}\sum_n k_n^+ a_{\mathrm{s}}^p + V_{\mathrm{m}}\sum_n k_n^+\exp\left[-\frac{V_{\mathrm{m}}}{RT}\left(\frac{\sigma_{\mathrm{eff}}}{R_{\mathrm{c}}}-p_{\mathrm{w}}\right)\right]\frac{Q}{K_{\mathrm{eq}}}\right\}\mathrm{d}t\\&= \frac{1}{2}\int_{b^{\mathrm{p}}_{\mathrm{m0}}}^{b^{\mathrm{p}}_{\mathrm{m}}}\exp\left[-\frac{V_{\mathrm{m}}}{RT}\left(\frac{\sigma_{\mathrm{eff}}}{R_{\mathrm{c}}}-p_{\mathrm{w}}\right)\right]\mathrm{d}b^{\mathrm{p}}_{\mathrm{m}}.\end{aligned} \tag{4.12}$$

The first-order approximation of the solution, obtained from equation (4.11) along with equation (4.12), reads

$$\begin{aligned} b_{\mathrm{m}}^{\mathrm{p}} \exp\left[-\frac{V_{\mathrm{m}}}{RT}\left(\frac{\sigma_{\mathrm{eff}}}{R_{\mathrm{c}}^{\mathrm{ref}}}-p_{\mathrm{w}}\right)\right] &= b_{\mathrm{m0}}^{\mathrm{p}} \exp\left[-\frac{V_{\mathrm{m}}}{RT}\left(\frac{\sigma_{\mathrm{eff}}}{R_{\mathrm{c0}}}-p_{\mathrm{w}}\right)\right] \\ &+ \left(R_{\mathrm{c}}^{\mathrm{ref}}-R_{\mathrm{c0}}\right) b_{\mathrm{m0}}^{\mathrm{p}} \exp\left[-\frac{V_{\mathrm{m}}}{RT}\left(\frac{\sigma_{\mathrm{eff}}}{R_{\mathrm{c0}}}-p_{\mathrm{w}}\right)\right] \frac{\sigma_{\mathrm{eff}} V_{\mathrm{m}}}{R_{\mathrm{c0}}^2 RT} \\ &+ \left(b_{\mathrm{m}}^{\mathrm{p}}-b_{\mathrm{m0}}^{\mathrm{p}}\right) \exp\left[-\frac{V_{\mathrm{m}}}{RT}\left(\frac{\sigma_{\mathrm{eff}}}{R_{\mathrm{c0}}}-p_{\mathrm{w}}\right)\right]. \end{aligned} \tag{4.13}$$

The first right-hand-side term indicates the onset of pressure solution creep. The following first-order terms respectively represent the move of the closed reaction system toward chemical equilibrium by stress transfer across expanding contacts and by concentration build-up in the interlayer. It does not make physical sense to call for higher-order terms which are approachable though.

Equation (4.13) shows in ultimate form as $b_{\mathrm{m}}^{\mathrm{p}}/b_{\mathrm{m0}}^{\mathrm{p}} = f\left(R_{\mathrm{c}}^{\mathrm{ref}}, \sigma_{\mathrm{eff}}, V_{\mathrm{m}}, T, R_{\mathrm{c0}}\right)$ (see Figure 1)

$$\frac{b_{\mathrm{m}}^{\mathrm{p}}}{b_{\mathrm{m0}}^{\mathrm{p}}} = \exp\left[-\frac{\sigma_{\mathrm{eff}} V_{\mathrm{m}}}{RT}\left(\frac{1}{R_{\mathrm{c0}}}-\frac{1}{R_{\mathrm{c}}^{\mathrm{ref}}}\right)\right] \frac{\dfrac{\sigma_{\mathrm{eff}} V_{\mathrm{m}}}{R_{\mathrm{c0}}^2 RT}\left(R_{\mathrm{c}}^{\mathrm{ref}}-R_{\mathrm{c0}}\right)}{1-\exp\left[-\dfrac{\sigma_{\mathrm{eff}} V_{\mathrm{m}}}{RT}\left(\dfrac{1}{R_{\mathrm{c0}}}-\dfrac{1}{R_{\mathrm{c}}^{\mathrm{ref}}}\right)\right]}, \tag{4.14}$$

with a complementary constraint on the upper limit

$$R_{\mathrm{c0}} \leq R_{\mathrm{c}}^{\mathrm{ref}} \leq R_{\mathrm{c}}^{\mathrm{eq}}. \tag{4.15}$$

The upper limit $R_{\mathrm{c}}^{\mathrm{eq}}$ can be determined by solving the partial derivative of equation (4.14) with respect to the variable $R_{\mathrm{c}}^{\mathrm{ref}}$

$$f'_{R_{\mathrm{c}}^{\mathrm{ref}}}\left(R_{\mathrm{c}}^{\mathrm{ref}}, \sigma_{\mathrm{eff}}, V_{\mathrm{m}}, T, R_{\mathrm{c0}}\right) = 0 \;\rightarrow\; R_{\mathrm{c}}^{\mathrm{eq}}. \tag{4.16}$$

The upper limit represents the extent to which contact area expansion will cease in the context of pressure solution creep and further when the closed system is at chemical compaction equilibrium.

The critical nonhydrostatic stress is then given as

$$\sigma_{\mathrm{n}}^{\mathrm{eq}} = \frac{\sigma_{\mathrm{eff}}}{R_{\mathrm{c}}^{\mathrm{eq}}} - p_{\mathrm{w}}. \tag{4.17}$$

As yet the critical nonhydrostatic stress is normally estimated from the latent heat of fusion (Stephenson et al., 1992; Revil, 1999)

$$\sigma_{\mathrm{n}}^{\mathrm{eq}} = \frac{E_m\left(1-T/T_m\right)}{4V_{\mathrm{m}}}, \tag{4.18}$$

where E_m [J/mol] and T_m [K] are the heat and temperature of fusion.

Based upon the reference closure characteristic curve which is at the disposal, three dimensionless geometry factors α, β, and θ [-] are called to reproduce

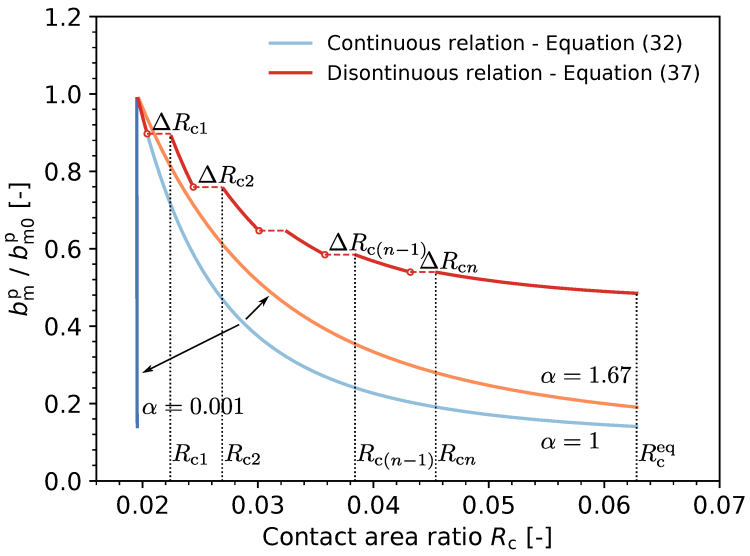

Figure 1: Move of the closed reaction system toward chemical equilibrium as a combined consequence of stress transfer across expanding contacts and concentration build-up in the interlayer

the real-world closure characteristic curve. Equation (4.14) is thus rewritten as (see Figure 1)

$$\frac{b_m^p}{b_{m0}^p} = \exp\left[-\frac{\sigma_{eff} V_m \beta}{RT}\left(\frac{1}{R_{c0}} - \frac{1}{R_c^{ref}}\right)\right] \frac{\theta \frac{\sigma_{eff} V_m}{R_{c0}^2 RT}\left(R_c^{ref} - R_{c0}\right)}{1 - \exp\left[-\frac{\sigma_{eff} V_m}{RT}\left(\frac{1}{R_{c0}} - \frac{1}{R_c^{ref}}\right)\right]}, \tag{4.19}$$

along with

$$\Delta R_c = \alpha \cdot \Delta R_c^{ref}. \tag{4.20}$$

The geometry factor α corrects the incremental contact area for the morphological difference, while the other two account for the independent contacts probably formed in aperture closure. Detailed specifications on the geometry factors are attached in Appendix 9.1.

5

REACTIVE SOLUTE TRANSPORT IN FRACTURES

5.1 CHANNELLING FLOW

Low-velocity channelling flow in rough-walled fractures is treated as steady-state laminar flow with no gravitational effects. For holding on to the classic parallel plate model, cubic law is assembled into the governing equation (Witherspoon et al., 1980)

$$\nabla \cdot \left(-\frac{b_{\mathrm{h}}^3}{12\eta} \nabla p_{\mathrm{w}} \right) = 0, \tag{5.1}$$

where b_{h} [m] is the hydraulic aperture parametrizing synthesized hydraulic characteristic of channelling flow, and η [Pa·s] is the fluid dynamic viscosity.

The hydraulic aperture b_{h} integrating spatial complexity of path tortuosity with channel topography can be estimated by combination of regular representative geometric parameters (Walsh, 1981)

$$b_{\mathrm{h}}^3 = \frac{1 - R_{\mathrm{c}}}{1 + R_{\mathrm{c}}} \, b_{\mathrm{m}}^3. \tag{5.2}$$

Following on the solution of hydraulic pressure field, the flow velocity $\mathbf{v}$ [m/s] is calculated

$$\mathbf{v} = -\frac{b_{\mathrm{h}}^2}{12\eta} \nabla p_{\mathrm{w}}. \tag{5.3}$$

5.2 REACTIVE SOLUTE TRANSPORT

Surface weathering takes place everywhere in through-going fractures due to mineral dissolution. The dissolution reactions take the general form

$$\bar{\mathbf{X}} + \mathbf{m}\, \mathrm{H_2O} \leftrightarrow \mathbf{s}\, \mathbf{X}, \tag{5.4}$$

where $\bar{\mathbf{X}} = \left(\bar{X}_1, \ldots, \bar{X}_i\right)^{\mathrm{T}}$, $\mathbf{X} = \left(X_1, \ldots, X_j\right)^{\mathrm{T}}$ represent vectorized mineral reactants and solutes, $\mathbf{m} = \left(m_1, \ldots, m_i\right)^{\mathrm{T}}$, $\mathbf{s} = \left[\left(s_{11}, \ldots, s_{i1}\right)^{\mathrm{T}}, \ldots, \left(s_{1j}, \ldots, s_{ij}\right)^{\mathrm{T}}\right]$ are the I-by-1 and I-by-J stoichiometric matrices.

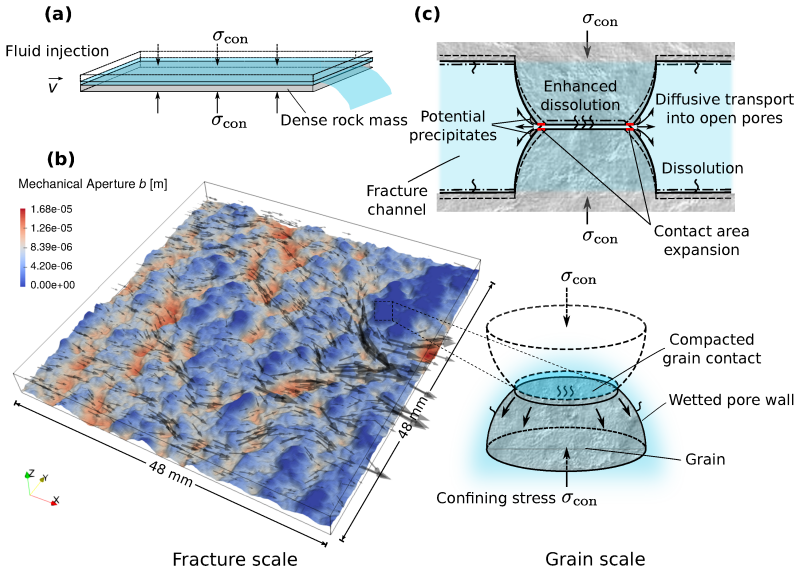

Figure 2: Schematic diagram of chemical compaction in a through-going fracture: (a) Geofluid streaming through out of a fractured dense rock mass under confining stress. (b) Channelling flow with surface weathering both inside and outside asperity contacts. (c) Pore volume reduction and contact area expansion due to pressure solution creep.

Given concentration enrichment by mass removal both inside and outside asperity contacts, solute transport in through-going fractures is described by advection-dispersion-reaction equation (see Figure 2)

$$b_{\mathrm{m}}\frac{\partial C_j}{\partial t}+\nabla\cdot\left(-b_{\mathrm{m}}\mathbf{D}\nabla C_j+b_{\mathrm{m}}\mathbf{v}C_j\right)=2f_{\mathrm{r}}^{'}\sum_{i=1}^{i}s_{ij}\left[\left(1-R_{\mathrm{c}}\right)\phi_i^{\mathrm{p}}\dot{m}_i^{\mathrm{p}}+f_{\mathrm{r},i}R_{\mathrm{c}}\phi_i^{\mathrm{c}}\dot{m}_i^{\mathrm{c}}\right], \tag{5.5}$$

where C_j [mol/m^3] is the solute concentration in terms of a particular species X_j, $\mathbf{D}$ [m^2/s] is the dispersion tensor, s_{ij} is the component of stoichiometric matrix $\mathbf{s}$, $f_{\mathrm{r}}^{'}$ [-] is the fracture surface roughness factor, i.e. the geometric area ratio of fracture surface over fracture surface plane, f_{r} [-] is the intragranular roughness factor, i.e. the ratio of authentic (total) grain surface area over apparent (geometric) grain surface area, ϕ_i^{c} and ϕ_i^{p} [-] are the area fractions of constituent mineral $\bar{X}_i$ with respect to asperity contacts and non-contact surfaces, $\dot{m}_i^{\mathrm{c}}$ and $\dot{m}_i^{\mathrm{p}}$ [mol/m^2/s] are the normalized mass removal rates inside and outside the contacts, determined by equation (3.1). Reaction-related terms have doubled since mass removal sources from opposing fracture surfaces. Note that the formulated governing equation omits the rate-limiting effect of diffusive transfer through out of the contacts.

The dispersion tensor $\mathbf{D}$ is given as (Scheidegger, 1961)

$$\mathbf{D}=D_{\mathrm{m}}\mathbf{I}+\alpha_{\mathrm{T}}|\mathbf{v}|\mathbf{I}+\left(\alpha_{\mathrm{L}}-\alpha_{\mathrm{T}}\right)\frac{\mathbf{v}^{\mathrm{T}}\mathbf{v}}{|\mathbf{v}|}, \tag{5.6}$$

with the molecular diffusion coefficient D_{m} [m^2/s], the longitudinal and transversal dispersion coefficients α_{L}, α_{T} [m].

The intragranular roughness factor f_r can be estimated via Brunauer-Emmet-Teller (BET) analysis of N_2 adsorption experiments (Tester et al., 1994)

$$f_r = \frac{S_{BET}}{S_{GEO}} = \frac{S_{BET}\, d\, \rho_m}{6}, \tag{5.7}$$

where S_{BET} [m^2/kg] is the specific surface area of grains measured from nitrogen adsorption isotherms, S_{GEO} [m^2/kg] is the specific geometric surface area of ideally smooth spherical grains, d [m] is the grain diameter, and ρ_m [kg/m^3] is the mineral density.

The area fractions of constituent minerals ϕ_i^p and ϕ_i^c are defined as

$$\phi_i^p = \frac{A_i^p}{A^p} \qquad \phi_i^c = \frac{A_i^c}{A^c}. \tag{5.8}$$

The effective surface area is not invariant but strongly related to such factors as grain morphology, pH and hydrothermal conditions, as well as the distance from equilibrium, though a consensus on this point has not yet been reached. Gautier et al. (2001) reported in their experimental investigation of quartz dissolution in natural systems that grain surface subjected to chemical weathering may contain substantial unreactive etch pits due to diffusion-dominated dissolution heterogeneity. Such advanced understanding on surface dissolution is in favor of adopting apparent surface area as the effective surface area for the process outside asperity contacts. On the other hand, loading of nonhydrostatic stress may prevail reactive sites over the asperity contacts, which justifies substitution by the authentic surface area.

5.3 HYDRAULIC FEEDBACK ON SURFACE DISSOLUTION

Surface retreat processes inside and outside asperity contacts have absolutely opposite effects on channel topography, despite the collective contribution to concentration enrichment. Surface retreat over asperity contacts guides the flow channel toward closure and causes contact area expansion in opposition to the retreat over non-contact surfaces. The combined effect of the surface retreat processes determines hydraulic evolution of channelling flow.

The representative hydraulic parameter b_h is normally associated with the mean aperture b_m and contact area ratio R_c (c.f. equation (5.2)). Since it has been creatively addressed interaction between channel topography and surface retreat over asperity contacts by means of the closure characteristic curve which introduces averaged non-zero aperture b_m^p instead of the regular representative geometric parameter b_m (see Chapter 4), we pay attention to the second contribution by surface retreat over non-contact surfaces and make efforts to fill in the gap between the intermediate parameter b_m^p and hydraulic parameter b_h.

Taking the time derivative of equation (4.4) yields

$$\dot{b}_m = (1 - R_c)\, \dot{b}_m^p - \dot{R}_c\, b_m^p. \tag{5.9}$$

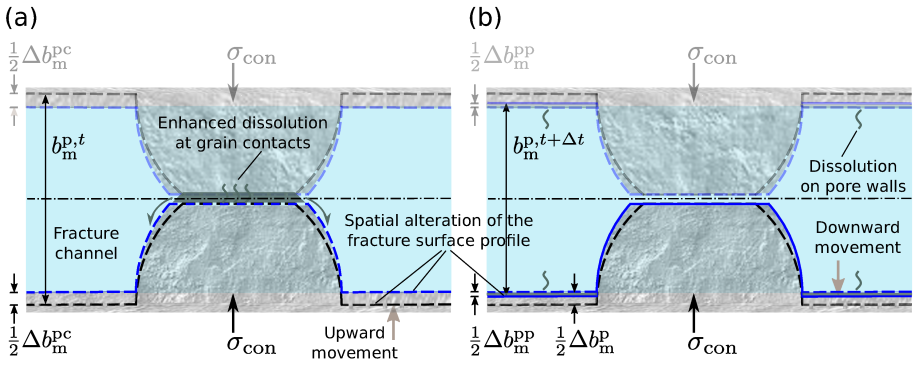

Figure 3: Schematic diagram of dissolution-induced alteration in channel topography: (a) due to the surface retreat over asperity contacts (b) due to the surface retreat over non-contact surfaces. The lines in black dashed, blue solid, and blue dashed represent the fracture surface profiles before and after the surface retreat processes, and in-between.

The rate of change of mean aperture $\dot{b}_\mathrm{m}$ [m/s] is expressed as a combination of the rates of change of contact area ratio $\dot{R}_\mathrm{c}$ [1/s] and averaged non-zero aperture $\dot{b}_\mathrm{m}^\mathrm{p}$ [m/s] which further decomposes into (see Figure 3)

$$\dot{b}_\mathrm{m}^\mathrm{p} = \dot{b}_\mathrm{m}^\mathrm{pp} + \dot{b}_\mathrm{m}^\mathrm{pc}, \tag{5.10}$$

where $\dot{b}_\mathrm{m}^\mathrm{pc}$ and $\dot{b}_\mathrm{m}^\mathrm{pp}$ [m/s] are the two components in response to surface retreat processes inside and outside asperity contacts. Another component accounting for cementation of secondary precipitates has been removed from equation (5.10) without consideration.

Given mineralogical complexity over non-contact surfaces and associated with the normalized mass removal rates of constituent minerals $\dot{m}_i^\mathrm{p}$, the component $\dot{b}_\mathrm{m}^\mathrm{pp}$ takes the form

$$\frac{1}{2}\,\dot{b}_\mathrm{m}^\mathrm{pp} = \frac{1}{A^\mathrm{p}} \int_{A^\mathrm{p}} \frac{1}{2}\,\dot{b}\,\mathrm{d}A = \sum_{i=1}^{i} \phi_i^\mathrm{p}\, \frac{1}{A_i^\mathrm{p}} \int_{A_i^\mathrm{p}} \frac{1}{2}\,\dot{b}\,\mathrm{d}A = \sum_{i=1}^{i} \phi_i^\mathrm{p}\, \frac{1}{f_{\mathrm{r},i}}\, V_{\mathrm{m},i}\, \dot{m}_i^\mathrm{p}. \tag{5.11}$$

To reach the ultimate expression, symmetry of the problem is exploited. Domain decomposition is in accordance with mineralogical composition over the non-contact surfaces. The surface integral over unreactive sites vanishes. The product of molar volume $V_{\mathrm{m},i}$ [m^3/mol] and normalized mass removal rate $\dot{m}_i^\mathrm{p}$ [mol/m^2/s] represents average surface retreat rate at the reactive sites (Lüttge et al., 1999).

Likewise, the component $\dot{b}_\mathrm{m}^\mathrm{pc}$ has

$$\frac{1}{2}\,\dot{b}_\mathrm{m}^\mathrm{pc} = -\sum_{i=1}^{i} \phi_i^\mathrm{c}\, V_{\mathrm{m},i}\, \dot{m}_i^\mathrm{c}. \tag{5.12}$$

Substituting equations (5.11) and (5.12) into equation (5.10) produces

$$\frac{1}{2}\,\dot{b}_\mathrm{m}^\mathrm{p} = \sum_{i=1}^{i} \phi_i^\mathrm{p}\, \frac{1}{f_{\mathrm{r},i}}\, V_{\mathrm{m},i}\, \dot{m}_i^\mathrm{p} - \sum_{i=1}^{i} \phi_i^\mathrm{c}\, V_{\mathrm{m},i}\, \dot{m}_i^\mathrm{c}. \tag{5.13}$$

So far alteration of channel topography has been well associated with diverse surface retreat processes, particularly in aperture variation. The components $\dot{b}_{\mathrm{m}}^{\mathrm{pp}}$ and $\dot{b}_{\mathrm{m}}^{\mathrm{pc}}$ along with the overall rate $\dot{b}_{\mathrm{m}}^{\mathrm{p}}$ can be directly calculated from the mass removal rates $\dot{m}_i^{\mathrm{p}}$, $\dot{m}_i^{\mathrm{c}}$.

Surface retreat over non-contact surfaces plays a minor role in the development of contact area, resisting contact area expansion by sharpening shape of grains in contact and shrinking independent contacts probable formed in aperture closure. Thus, it is reliable enough to estimate contact area expansion based upon the closure characteristic curve. The limited negative effect on contact area expansion can be made by tweaking the geometry factors in equation (4.19).

Part III

SIMULATION

6

MODELING

6.1 PROBLEM DESCRIPTION

A typical flow-through experiment was conducted by Yasuhara et al. (2011), where a centrally bisected granite core sample was exposed to confining stress of 5 MPa, ambient temperatures of 25°C and 90°C, and differential hydraulic pressures of 0.04 MPa and 0.1 MPa. Deionized water was streaming through out of an artificially induced fracture of 61.2 mm in length and 29.4 mm in width. Volumetric outflow rate was real-time logged by weighing effluent. Element concentrations were periodically measured after fluid sampling from the effluent. Amorphous silica and calcite were detected in the examination of precipitation post the flow-through experiment.

Figure 4 shows the fracture permeability evolution in form of hydraulic aperture. Hydraulic aperture was calculated from measured volumetric outflow rate $Q_{\text{out}}^{\text{meas}}$ [m^3/s], via the cubic law (Witherspoon et al., 1980)

$$b_{\text{h}} = \left(\frac{12\eta \cdot Q_{\text{out}}^{\text{meas}}}{w \cdot \nabla p_{\text{w}}} \right)^{1/3}, \tag{6.1}$$

with the fracture width w [m]. Hydraulic aperture decreases from approximately 9 µm to 1.6 µm under varying hydrothermal conditions. Reduction rate of hydraulic aperture becomes greater with temperature elevation from 25°C to 90°C. Increasing differential hydraulic pressure from 0.04 MPa to 0.1 MPa slightly raises the hydraulic aperture.

Figures 5 shows the evolution of effluent element concentrations including Si, Al, K, Fe, Ca, Na, and Mg. Element concentrations keep stable at varying temperatures and have stepwise increases by thermal stimulation. The finding of calcite in the post-examination indicates dissolved carbon dioxide was unexpectedly blended into the inflow.

6.2 MODEL SETUP

A parallel computing 1-D reactive transport model is implemented into the FEM-based simulator OpenGeoSys (Kolditz et al., 2012) integrated with

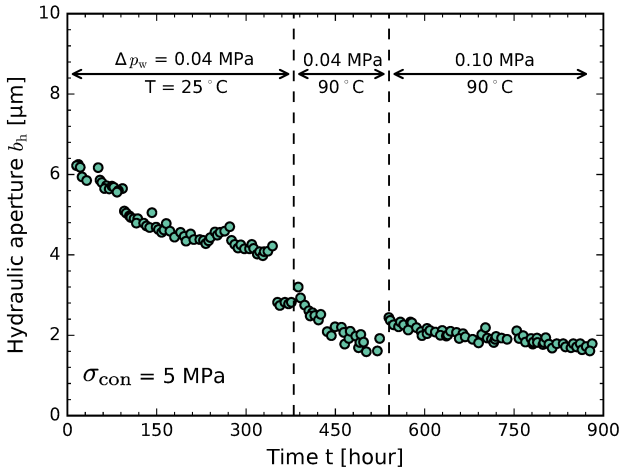

Figure 4: Measured fracture permeability evolution under prescribed crustal conditions, presented in form of hydraulic aperture (Yasuhara et al., 2011).

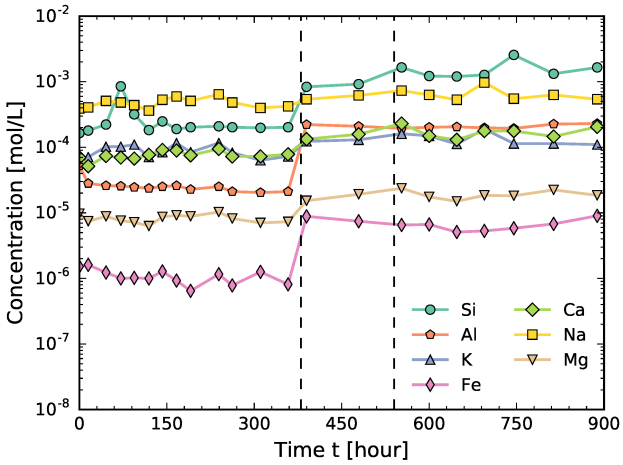

Figure 5: Measured evolution of effluent element concentrations (Yasuhara et al., 2011).

IPhreeqc module for speciation calculation (Charlton and Parkhurst, 2011; He et al., 2015).

6.2.0.1 *Model settings for channelling flow and solute transport*

The throughgoing fracture is represented as a one-dimensional entity discretized with 60 line elements. Each element has a length of 1.02 mm. Inflow and outflow pressures are prescribed as 0.04 MPa | 0.1 MPa and 0 MPa. Element concentrations at the inlet are held at zero. A small fixed time step size Δt = 0.004 s is adopted at the onset and in the interim, otherwise the step size is adjusted to 1.2 s. Hydraulic pressure field and concentration field are solved with a uniform relative convergence tolerance of 10^{-16}.

The initial contact area ratio R_{c0} is arbitrarily set to 1.95 %, because of unavailability of actual fracture channel topography (Luo et al., 2017). The mean mechanical aperture b_m is initialized to 9.12 μm, via equation (5.2). The homogenized molar volume V_m^{hom} = 6.57 × 10^{-5} m^3/mol is calculated based upon mineralogical composition of Mizunami granite. Main physical properties of the constituent minerals are listed in Table 1. Parametric settings for 1-D reactive transport model are summarized in Table 3.

The closure characteristic curve used in the simulation takes the form

$$\frac{b_m^p}{b_{m0}^p} = \exp\left[-\frac{\sigma_{eff} V_m^{hom} \beta}{RT}\left(\frac{1}{R_{c0}} - \frac{1}{R_c}\right)\right] \frac{\theta \frac{\sigma_{eff} V_m^{hom}}{R_{c0}^2 RT}\left(R_c - R_{c0}\right)}{1 - \exp\left[-\frac{\sigma_{eff} V_m^{hom}}{RT}\left(\frac{1}{R_{c0}} - \frac{1}{R_c}\right)\right]}, \tag{6.2}$$

which is modified from equation (4.19) in use for polymineralic systems. The geometry factors α, β, and θ are all set to unity. Taking advantage of α = 1.0, R_c^{ref} is replaced with R_c. The other parameters used for curve generation are given as follows: b_{m0}^p = 9.3 μm, σ_{eff} = 5 MPa, V_m^{hom} = 6.57 × 10^{-5} m^3/mol, T = 298 K | 363 K, and R_{c0} = 1.95%.

6.2.0.2 *Model settings for speciation calculation*

Water-granite interaction involves kinetic dissolution reactions (see Table 4), considerable equilibrium aqueous reactions, and probably active precipitation reactions. Amorphous silica and gibbsite serve as secondary precipitates in configuring geochemical system which can be accounted for by diagnosis of secondary mineral paragenesis (Zhu and Lu, 2009; Lu et al., 2017), though there is no direct experimental evidence in support of this move. Dissolution kinetics datasets are listed in Table 2. Speciation calculation is based on the LLNL thermodynamic database. Furthermore, we move on using equation (4.18) for estimating the critical nonhydrostatic stress. Table 1 lists sets of mineral-specific critical nonhydrostatic stress and upper limit of contact area ratio.

Table 1: Mineralogical composition of Mizunami granite and main physical properties of constituent minerals

Mineral	ϕ	$^1\phi^{\mathrm{p}}$	$^1\phi^{\mathrm{c}}$	ρ_{m}	V_{m}	$^2f_{\mathrm{r}}$	^3E_m	^3T_m	$\sigma_{\mathrm{n}}^{\mathrm{eq}}$ [MPa]		$R_{\mathrm{c}}^{\mathrm{eq}}$ [%]	
	[%]	[%]	[%]	[g/cm^3]	[m^3/mol]	[-]	[KJ/mol]	[K]	25°C	90°C	25°C	90°C
Quartz	50	50	50	2.65	2.27×10^{-5}	40.10	8.57	1883	79.45	76.19	6.29	6.56
K-feldspar	25	25	25	2.55	1.09×10^{-4}	38.58	57.74	1473	105.63	99.80	4.73	5.01
Albite	10	10	10	2.62	1.00×10^{-4}	39.64	62.76	1373	122.83	115.42	4.07	4.33
Anorthite	10	10	10	2.75	1.01×10^{-4}	41.61	133	1830	275.57	263.91	1.81	1.89
Biotite	5	5	5	2.10	1.40×10^{-4}	31.77	/	/	/	/	/	/

[1] Assumed in conformity with the overall mineralogical configuration.

[2] Calculated by equation (5.7). The grain diameter d = 178 μm and BET surface area S_{BET} = 0.51 m^2/g source from Yasuhara et al. (2011).

[3] Data source: quartz - from Stephenson et al. (1992); k-feldspar and albite - from Stebbins et al. (1983); anorthite - Lange et al. (2009); biotite - not found.

Table 2: Dissolution kinetics data

Mineral	Acid			Neutral		Base		
	$\log k_1$	n_1	E_1	$\log k_2$	E_2	$\log k_3$	n_3	E_3
Quartz	/	/	/	-13.99	87.7	/	/	/
K-feldspar	-10.06	0.500	51.7	-12.41	38.0	-21.20	-0.823	94.1
Albite	-9.87	0.457	65.0	-12.04	69.8	-16.98	-0.572	71.0
Anorthite	-3.32	1.5	18.4	-11.6	18.4	-13.5	-0.33	18.4
Biotite	-9.84	0.525	22.0	-12.55	22.0	/	/	/

Data source: anorthite - from Li et al. (2006); the others - from Palandri and Kharaka (2004).

Table 3: Parametric settings for 1-D reactive transport simulation

Parameter	Value	Unit
Confining stress σ_{con}	5	MPa
Length of the fracture l	61.2	mm
Initial contact area ratio R_{c0}	1.95	%
Initial mean mechanical aperture b_{m0}	9.12	μm
Initial averaged non-zero mechanical aperture $b^{\mathrm{p}}_{\mathrm{m0}}$	9.3	μm
Homogenized molar volume $V^{\mathrm{hom}}_{\mathrm{m}}$	6.57×10^{-5}	$\mathrm{m^3/mol}$
Geometry factors α, β, and γ	1.0	/
Water dynamic viscosity η	9×10^{-4} (25°C)	Pa·s
	3.15×10^{-4} (90°C)	Pa·s
Molecular diffusion coefficient D_{m}	2.24×10^{-10} (25°C)	$\mathrm{m^2/s}$
	5.94×10^{-10} (90°C)	$\mathrm{m^2/s}$
Longitudinal dispersion coefficient α_{L}	0.001	m
[1]Fracture surface roughness factor $f^{'}_{\mathrm{r}}$	1.0	-
Element length Δx	1.02	mm
Time step size Δt	0.004 | 1.2	s

[1] Estimated from numerically generated fracture surface topography (Sidick, 2009; Lu et al., 2017).

Table 4: Calibrated reaction configurations for geochemical system

Mineral	Chemical reaction
Quartz	SiO_2+2 $H_2O \rightarrow H_4SiO_4$
K-feldspar	$KAlSi_3O_8 + 4\,H^+ + 4\,H_2O \rightarrow Al^{3+} + K^+ + 3\,H_4SiO_4$
Albite	$NaAlSi_3O_8 + 4\,H^+ + 4\,H_2O \rightarrow Al^{3+} + Na^+ + 3\,H_4SiO_4$
Anorthite	$CaAl_2(SiO_4)_2 + 8\,H^+ \rightarrow 2\,Al^{3+} + Ca^{2+} + 2\,H_4SiO_4$
Biotite	[5 Phlogopite : 1 Annite] + $10\,H^+ \rightarrow Al^{3+} + K^+ + 2.5\,Mg^{2+} + 0.5\,Fe^{2+} + 3\,H_4SiO_4$
Amorphous silica	$SiO_2 + 2\,H_2O \leftrightarrow H_4SiO_4$(am)
Gibbsite	$Al^{3+} + 3\,H_2O \leftrightarrow Al(OH)_3 + 3\,H^+$

Note. Biotite in examination consists of phlogopite $KAlMg_3Si_3O_{10}(OH)_2$ and annite $KFe_3AlSi_3O_{10}(OH)_2$ with a mixing ratio of 5 : 1.

7

RESULTS AND DISCUSSION

7.1 COMPARISON AGAINST LABORATORY EXPERIMENTS

Figure 6 and Figure 7 present predicted evolutions of fracture permeability and effluent element concentrations along with the experimental data. Overall, the serial predictions are consistent with the measurements. The good agreement has proven the success in reactive transport modeling, particularly in the mechanistic model development. The updated reactive transport model is allowed to precisely capture the strong interaction between channelling flow and pressure solution creep. Despite great advancement in addressing hydro-chemical coupling problems within deformable fractures, localized discrepancies against the measurements draws more attentions. The discrepancy of hydraulic aperture in the initial dozens of hours may result from the attendant mechanical mechanisms. Fracture reopening has not been captured since the pressurization-induced lifting effect was beyond the consideration of the present model. Ca concentration is underestimated throughout the simulation, probably because concentration enrichment by mass removal from anorthite contacts was taken out. The considerable discrepancy in K concentration may arise from the the overestimation to the critical nonhydrostatic stress.

7.2 INSIGHTS INTO FRACTURE PERMEABILITY EVOLUTION

Surface retreat over asperity contacts undergoes two main phases during fracture permeability evolution. Diverse mechanical mechanisms (e.g., undercutting and stress corrosion) and pressure solution are jointly contributed to the fast-decreasing fracture permeability at early age via surface retreat over asperity contacts — approximately two-fifth of the total net reduction of hydraulic aperture within the initial dozens of hours. Followed by the steep decline, pressure solution becomes the unique driving mechanism for surface retreat over asperity contacts until compaction equilibrium is reached. Pressure solution in progress is accompanied by contact area expansion which reversely makes attenuation of pressure solution by stress transfer. The hydraulic aperture consequently slopes down towards convergence. Temper-

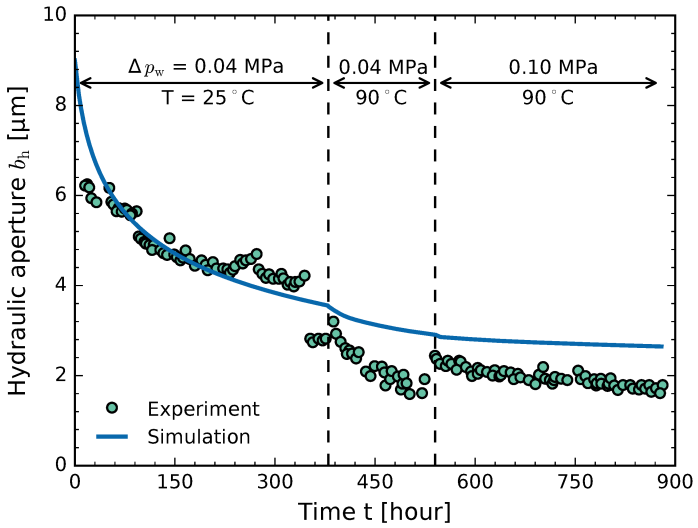

Figure 6: Comparison against the experimental measurements in terms of fracture permeability evolution.

ature elevation greatly contributes to accelerating the progression of pressure solution creep with no effect on prolongation of the lifespan of the process.

7.3 INSIGHTS INTO ELEMENT CONCENTRATION EVOLUTIONS

The present experimental or numerical results in terms of effluent element concentrations are several orders of magnitude higher than those measured under hydrostatic pressure (Worley, 1994), thereby confirming the phenomena of dissolution enhancement over nonhydrostatically stressed solids.

The measured effluent element concentrations waggle within a small range at varying temperatures, while those by model prediction (e.g. Na, K, Mg, and Fe concentrations) are subjected to quasi-exponential decay in each stage. The apparent concentration variation appears at temperature elevation from 25 °C to 90 °C, due to the thermally induced dissolution enhancement. Re-examining the entire concentration evolutions, we find the steady behavior at constant temperatures deserves serious consideration. The volumetric reduction of the flow channel and the prolonged traveling time within the fracture do not raise the effluent element concentrations as would normally be expected. The majority by model prediction even show a clear tendency to decrease in the initial dozens of hours while the hydraulic aperture drops down by approximately one-third. Actually, the hydraulic impacts on fluid chemistry in this context are masked by a competing mechanism. Contact area expansion makes attenuation of dissolution enhancement at asperity contacts, which compensates the volumetric reduction of the flow channel.

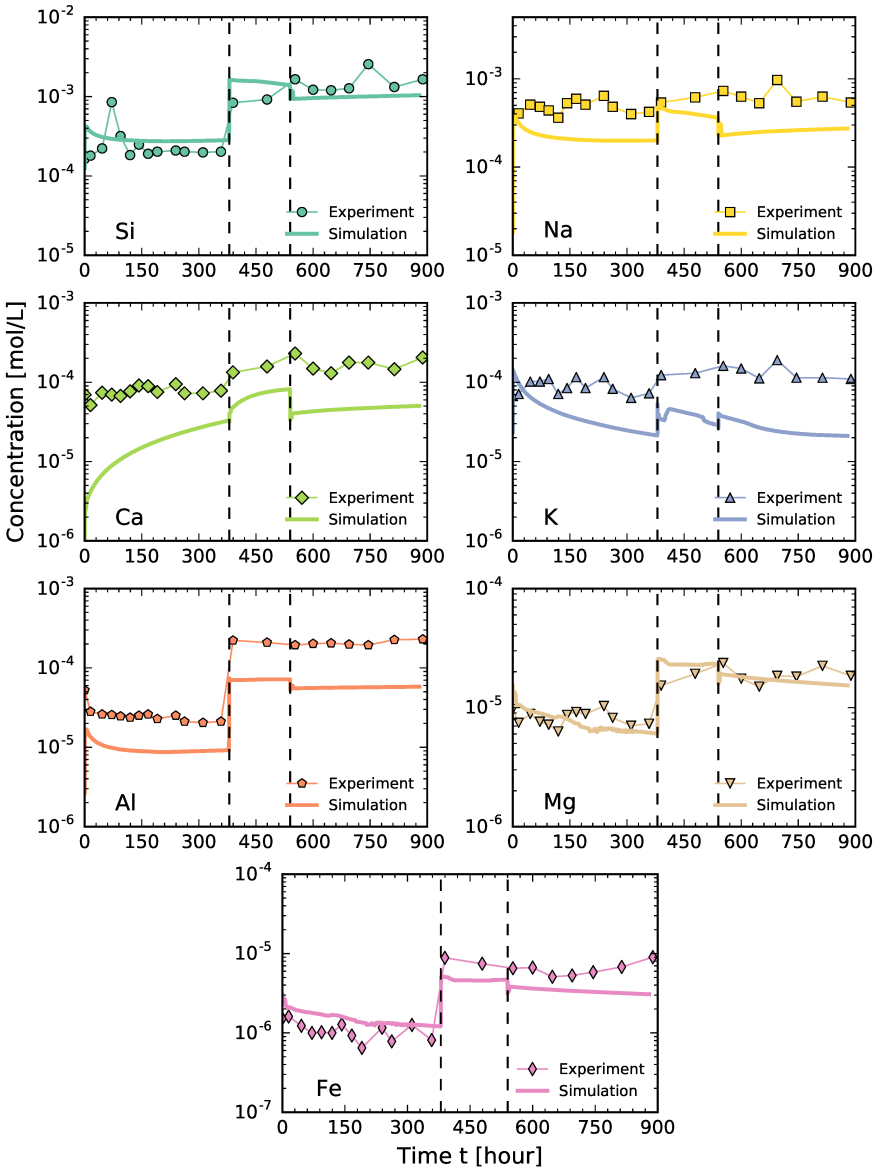

Figure 7: Comparison against the experimental measurements in terms of element concentration evolutions.

7.4 COMPARISON AGAINST EXISTING RELATIONS

Yasuhara, Hideaki and Elsworth, Derek and Polak, Amir (2004) gave a closure characteristic regression relationship which preserves the regular representative geometric parameters

$$b_{\mathrm{m}} = b_r + (b_{\mathrm{m0}} - b_r) \exp\left[-\left(R_{\mathrm{c}} - R_{\mathrm{c0}}\right)/\zeta\right], \tag{7.1}$$

where b_r [m] is the residual mean mechanical aperture, and ζ [-] is a fitting parameter.

Inserting equations (5.9) and (5.10) into equation (7.1) after taking the time derivative of both sides yields

$$\frac{1}{1-R_{\mathrm{c}}}\left\{b_{\mathrm{m}}^{\mathrm{p}} - \frac{b_{\mathrm{m0}} - b_r}{\zeta}\exp\left[-\left(R_{\mathrm{c}} - R_{\mathrm{c0}}\right)/\zeta\right]\right\}\dot{R}_{\mathrm{c}} = \dot{b}_{\mathrm{m}}^{\mathrm{pp}} + \dot{b}_{\mathrm{m}}^{\mathrm{pc}}. \tag{7.2}$$

The rate of change of contact area ratio $\dot{R}_{\mathrm{c}}$ is actually linked with the two components of the rate of change of averaged non-zero aperture in using the closure characteristic regression relationship. The first component $\dot{b}_{\mathrm{m}}^{\mathrm{pp}}$ as an average product is hard to be viewed as the local surface retreat around asperity contacts in cases of polymineralic systems which is the part of resisting contact area expansion in fracture closure. Furthermore, it may be too simplistic to describe contact area development in response to surface retreat both inside and outside asperity contacts in a uniform manner which are governed by varying dissolution mechanisms.

The closure characteristic relationship has been updated with a new appearance, characterized by the averaged non-zero aperture $b_{\mathrm{m}}^{\mathrm{p}}$ instead of the regular representative geometric parameter b_{m}. The redefined closure characteristic relationship is herein formulated by process-based generation approach, in association with the the dominant surface retreat process. The rate of change of contact area ratio $\dot{R}_{\mathrm{c}}$ is thus specified on the second component $\dot{b}_{\mathrm{m}}^{\mathrm{pc}}$ rather than on the overall rate $\dot{b}_{\mathrm{m}}^{\mathrm{p}}$. The philosophy of the process-based generation approach is to first prototype the real-world flow channel by generating a reference closure characteristics curve from the featured physical process, and then calibrate the reference closure characteristics curve toward the target configuration. Three dimensionless geometry factors α, β, and θ are called for filling in the gap between reference and target closure characteristic curves, accounting for the difference in fracture channel topography at varying length scales.

7.5 IMPACT OF FRACTURE CHANNEL TOPOGRAPHY

Fracture channel topography impacts on fracture permeability evolution (see Figure 8). With the decrease of initial contact area ratio, the reduction rate of fracture permeability turns out to be higher in the first phase and to be lower in the subsequent higher-temperature phase. The higher nonhydrostatic stress, the more active pressure solution creep. With approach of

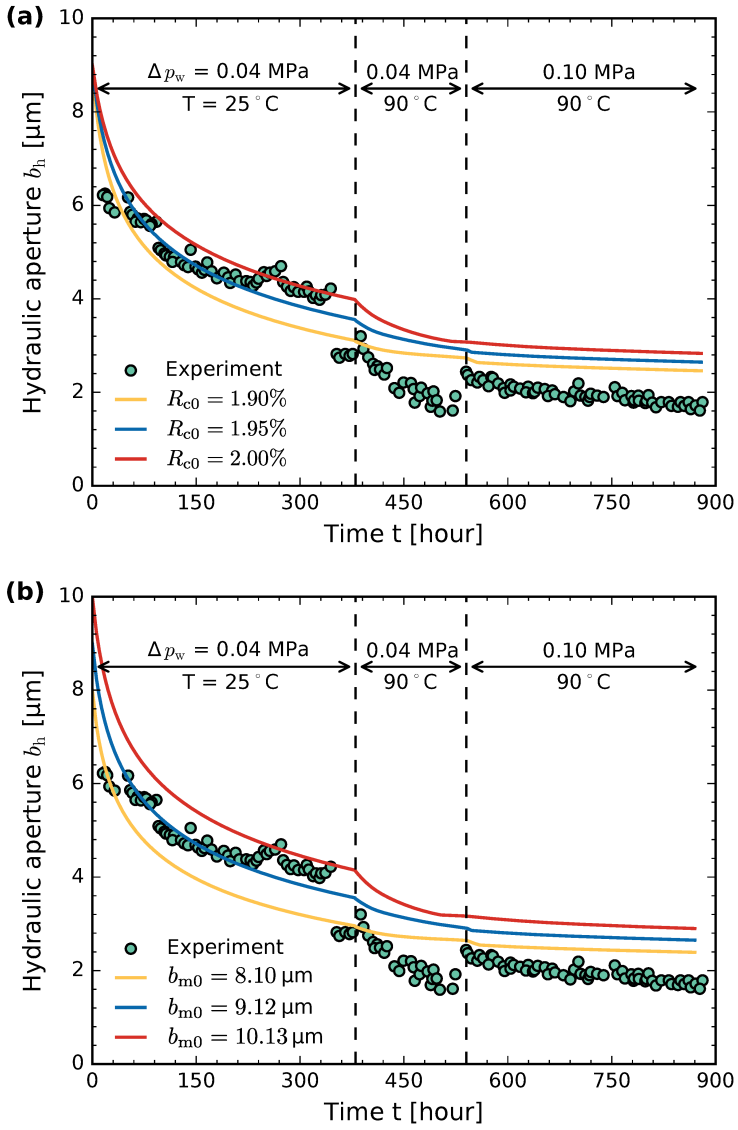

Figure 8: Impact of fracture channel topography on permeability evolution: (a) initial contact area ratio R_{c0} (b) initial mean aperture b_{m0}.

chemical compaction equilibrium, fracture permeability evolution becomes less sensitive to thermal stimulation.

Fracture permeability evolutions with the initial mean aperture increasing from 8 μm to 10 μm are converged by the end. Varying the mean aperture under a fixed contact area ratio acts like adjusting the geometry factor α which accounts for the impact of grain morphology.

Fracture surface roughness at varying length scales determines pressure solution creep in magnitude and rate of change (see Figure 1). Grain morphology has a significant effect on contact area expansion around those existing ones, while surface roughness at greater length scales intermittently and negatively intervenes pressure solution creep by forming new independent contacts in fracture closure.

Part IV

SUMMARY

8

CONCLUSIONS AND OUTLOOK

Advancing the understanding of pressure solution creep as a fundamental deformation mechanism in the upper crust has far-reaching implications for diagenetic compaction in sedimentary basins, interseimic healing and sealing of fault gouge, and reactive solute transport in deformable geomaterials.

For this purpose, this work puts forward a new mechanistic model of pressure solution creep which is developed based upon the classical thermodynamic model for describing stress-induced dissolution enhancement and the general reaction rate law for describing attenuation characteristic of pressure solution along with the hypothesis of closed system. The presented mechanistic model demonstrates that: (1) stress transfer across expanding contacts and concentration build-up in the interlayer of absorbed water slow down pressure solution creep over time; (2) the ceasing of pressure solution creep depends upon the concentration build-up in the interlayer which is constrained by the follow-up solute migration process; (3) solute migration process is a primary rate-limiting process of pressure solution creep.

This work then sheds light on hydro-chemical coupled problems in deformable fractures in the context of pressure solution creep. With the integration of the new mechanistic model into the reactive transport model, one is allowed to capture the strong interaction between channelling flow and pressure solution creep under crustal conditions. This numerical investigation provides a justified interpretation for the unusual experimental observation that fracture permeability reduction does not necessarily cause concentration enrichment. Contact area expansion makes attenuation of dissolution enhancement at asperity contacts, which compensates the volumetric reduction of the flow channel. Temperature elevation greatly contributes to accelerating the progression of pressure solution creep with no effect on prolongation of the lifespan of the process.

Part V

APPENDIX

9

APPENDIX

9.1 GEOMETRY FACTORS

The geometry factor α narrows the gap from the perspective of grain morphology. For an extreme case where columnar shaped grains prop fracture opening, the geometrical relation is shaped with $\alpha = 0.001$. $\alpha > 1$ suits for a situation where compacted grains have a more gentle surface slope than those in the prototyped fracture channel. The other two geometry factors β and θ give discontinuity of contact area expansion full consideration as a result of surface roughness at greater length scales. The increments at the discontinuity points functionally constrain the total amount of fracture closure.

$$\Delta R_{\mathrm{c}} = \frac{f'_{R_{\mathrm{c}}^{\mathrm{ref}}}\left(R_{\mathrm{c}}^{\mathrm{ref}}, \sigma_{\mathrm{eff}}, V_{\mathrm{m}}, T, R_{\mathrm{c0}}\right)}{f'_{R_{\mathrm{c}}}\left(R_{\mathrm{c}}\right)} \cdot \Delta R_{\mathrm{c}}^{\mathrm{ref}} = \alpha\left(R_{\mathrm{c}}, R_{\mathrm{c}}^{\mathrm{ref}}\right) \cdot \Delta R_{\mathrm{c}}^{\mathrm{ref}}. \tag{9.1}$$

As grain shape of those in contact turns sharper by water-rock interaction, surface retreat around the peripheries of grain contacts indirectly acts upon contact area expansion.

The newly inserted geometry factors β [-] and θ [-] are both expressed as piecewise functions of contact area ratio

$$\beta\left(R_{\mathrm{c}}^{\mathrm{ref}}\right) = \begin{cases} 1 & R_{\mathrm{c0}} \leq R_{\mathrm{c}}^{\mathrm{ref}} < R_{\mathrm{c1}} - \Delta R_{\mathrm{c1}} \\ 1 - \frac{\sum_{i=1}^{n}\left(\frac{1}{R_{\mathrm{c}i} - \Delta R_{\mathrm{c}i}} - \frac{1}{R_{\mathrm{c}i}}\right)}{\frac{1}{R_{\mathrm{c0}}} - \frac{1}{R_{\mathrm{c}}^{\mathrm{ref}}}} & R_{\mathrm{c}n} \leq R_{\mathrm{c}}^{\mathrm{ref}} < R_{\mathrm{c}(n+1)} - \Delta R_{\mathrm{c}(n+1)} \end{cases}, \tag{9.2}$$

$$\theta\left(R_{\mathrm{c}}^{\mathrm{ref}}\right)=\begin{cases}1, & \left(R_{\mathrm{c}0}\leq R_{\mathrm{c}}^{\mathrm{ref}}<R_{\mathrm{c}1}-\Delta R_{\mathrm{c}1}\right)\\ \prod_{i=0}^{n-1}\frac{\frac{\sigma_{\mathrm{eff}}V_{\mathrm{m}}}{R_{\mathrm{c}i}^{2}RT}\left(R_{\mathrm{c}(i+1)}-\Delta R_{\mathrm{c}(i+1)}-R_{\mathrm{c}i}\right)}{1-\exp\left[-\frac{\sigma_{\mathrm{eff}}V_{\mathrm{m}}}{RT}\left(\frac{1}{R_{\mathrm{c}i}}-\frac{1}{R_{\mathrm{c}(i+1)}-\Delta R_{\mathrm{c}(i+1)}}\right)\right]} & \\ \cdot\frac{\frac{1}{R_{\mathrm{c}n}^{2}}\left(R_{\mathrm{c}}^{\mathrm{ref}}-R_{\mathrm{c}n}\right)}{\frac{1}{R_{\mathrm{c}0}^{2}}\left(R_{\mathrm{c}}^{\mathrm{ref}}-R_{\mathrm{c}0}\right)}\cdot\frac{1-\exp\left[-\frac{\sigma_{\mathrm{eff}}V_{\mathrm{m}}}{RT}\left(\frac{1}{R_{\mathrm{c}0}}-\frac{1}{R_{\mathrm{c}}^{\mathrm{ref}}}\right)\right]}{1-\exp\left[-\frac{\sigma_{\mathrm{eff}}V_{\mathrm{m}}}{RT}\left(\frac{1}{R_{\mathrm{c}n}}-\frac{1}{R_{\mathrm{c}}^{\mathrm{ref}}}\right)\right]} & \\ \left(R_{\mathrm{c}n}\leq R_{\mathrm{c}}^{\mathrm{ref}}<R_{\mathrm{c}(n+1)}-\Delta R_{\mathrm{c}(n+1)}\right)\end{cases}, \tag{9.3}$$

with a series of discontinuity points of contact area ratio $R_{\mathrm{c}1}$, ..., $R_{\mathrm{c}(n+1)}$, and increments in the ratio at the discontinuity points $\Delta R_{\mathrm{c}1}$, ..., $\Delta R_{\mathrm{c}(n+1)}$. By definition, it is clear that the geometry factors β and θ, varying between 0 and 1, are determined by roughness of pristine surface topography as well as rate difference between the surface retreat on pore walls and at grain contacts. The progressive surface retreat on pore walls shrinks independent contacts being formed over the fracture surface.

9.2 PUBLICATIONS

Journal articles for this accumulative dissertation:

Lu, R., Nagel, T., Shao, H., Kolditz, O., & Shao, H. (2018). Modeling of dissolution-induced permeability evolution of a granite fracture under crustal conditions. *Journal of Geophysical Research: Solid Earth*, 123, 5609-5627. https://doi.org/10.1029/2018JB015702

Lu, R., Watanabe, N., He, W., Jang, E., Shao, H., Kolditz, O., & Shao H. (2017). Calibration of water-granite interaction with pressure solution in a flow-through fracture under confining pressure, *Environmental Earth Sciences*, 76, 417-430. https://doi.org/10.1007/s12665-017-6727-1

Other Journal articles:

Yoshioka, K., Parisio, F., Naumov, D., **Lu, R.**, Kolditz, O., & Nagel, T. (2019), Comparative verification of discrete and smeared numerical approaches for the simulation of hydraulic fracturing, GEM-International Journal on Geomathematics, 10(1), art. 13.

Bond, A.E., Bruský, I., Chittenden, N., Feng, X.-T., Kolditz, O., Lang, P., **Lu, R.**, McDermott, C., Neretnieks, I., Pan, P.-Z., Šembera, J., Shao, H., Yasuhara, H., & Zheng, H. (2016). Development of approaches for modelling coupled thermal-hydraulic-mechanical-chemical processes in single granite fracture experiment. *Environmental Earth Sciences*, 75(19), art. 1313.

Conference papers:

Bond, A.E., Chittenden, N., Fedors, R., Lang, P., McDermott, C., Neretnieks, I., Pan, P.-Z., Sembera, J., Brusky, I., Watanabe, N., **Lu, R.**, & Yasuhara, H. (2018). Coupled THMC modelling of single fractures in novaculite and granite. *International Discrete Fracture Network Engineering Conference*, Seattle, Washington, USA.

Book contributions:

Lu, R., Watanabe, N., Jang, E., & Shao, H. (2018) RTM processes. In: Kolditz, O., Nagel, T., Shao, H., Wang, W., Bauer, S., (eds.) Thermo-hydro-mechanical-chemical processes in fractured porous media: Modelling and benchmarking. Terrestrial Environmental Sciences. Springer, New York, 253-258.

Watanabe, N., **Lu, R.**, Taron, J., He, W., Jang, E., & Shao, H. (2016) Mechanical-chemical (MC) processes. In: Kolditz, O., Görke, U.-J., Shao, H., Wang, W., Bauer, S., (eds.) Thermo-hydro-mechanical-chemical processes in fractured porous media: Modelling and benchmarking. Terrestrial Environmental Sciences. Springer, New York, 199-209.

Enclosed Publication

[EP1] **Lu, R.**, Nagel, T., Shao, H., Kolditz, O., & Shao, H. (2018). Modeling of dissolution-induced permeability evolution of a granite fracture under crustal conditions. *Journal of Geophysical Research: Solid Earth*, 123, 5609-5627. https://doi.org/10.1029/2018JB015702

Enclosed Publication

[EP2] **Lu, R.**, Watanabe, N., He, W., Jang, E., Shao, H., Kolditz, O., & Shao H. (2017). Calibration of water-granite interaction with pressure solution in a flow-through fracture under confining pressure, *Environmental Earth Sciences*, 76, 417-430. https://doi.org/10.1007/s12665-017-6727-1

Enclosed Publication

[EP3] Yoshioka, K., Parisio, F., Naumov, D., **Lu, R.**, Kolditz, O., & Nagel, T. (2019), Comparative verification of discrete and smeared numerical approaches for the simulation of hydraulic fracturing, GEM-International Journal on Geomathematics, 10(1), art. 13.

LIST OF FIGURES

Figure 1 Move of the closed reaction system toward chemical equilibrium as a combined consequence of stress transfer across expanding contacts and concentration build-up in the interlayer 15

Figure 2 Schematic diagram of chemical compaction in a through-going fracture: (a) Geofluid streaming through out of a fractured dense rock mass under confining stress. (b) Channelling flow with surface weathering both inside and outside asperity contacts. (c) Pore volume reduction and contact area expansion due to pressure solution creep. 17

Figure 3 Schematic diagram of dissolution-induced alteration in channel topography: (a) due to the surface retreat over asperity contacts (b) due to the surface retreat over non-contact surfaces. The lines in black dashed, blue solid, and blue dashed represent the fracture surface profiles before and after the surface retreat processes, and in-between. 19

Figure 4 Measured fracture permeability evolution under prescribed crustal conditions, presented in form of hydraulic aperture (Yasuhara et al., 2011). 23

Figure 5 Measured evolution of effluent element concentrations (Yasuhara et al., 2011). 23

Figure 6 Comparison against the experimental measurements in terms of fracture permeability evolution. 28

Figure 7 Comparison against the experimental measurements in terms of element concentration evolutions. 29

Figure 8 Impact of fracture channel topography on permeability evolution: (a) initial contact area ratio R_{c0} (b) initial mean aperture b_{m0}. 31

LIST OF TABLES

Table 1 Mineralogical composition of Mizunami granite and main physical properties of constituent minerals 25
Table 2 Dissolution kinetics data 25
Table 3 Parametric settings for 1-D reactive transport simulation 26
Table 4 Calibrated reaction configurations for geochemical system 26

BIBLIOGRAPHY

Bernabé, Y and B Evans (2014). Pressure solution creep of random packs of spheres. *Journal of Geophysical Research: Solid Earth* 119 (5), pp. 4202–4218.

Bos, B. and C. J. Spiers (2002). Frictional-viscous flow of phyllosilicate-bearing fault rock: Microphysical model and implications for crustal strength profiles. *Journal of Geophysical Research: Solid Earth* 107 (B2).

Charlton, S. R. and D. L. Parkhurst (2011). Modules based on the geochemical model PHREEQC for use in scripting and programming languages. *Computers & Geosciences* 37 (10), pp. 1653–1663.

De Boer, R. (1977). On the thermodynamics of pressure solution–interaction between chemical and mechanical forces. *Geochimica et Cosmochimica acta* 41 (2), pp. 249–256.

Evans, J. P. and F. M. Chester (1995). Fluid-rock interaction in faults of the San Andreas system: Inferences from San Gabriel fault rock geochemistry and microstructures. *Journal of Geophysical Research: Solid Earth* 100 (B7), pp. 13007–13020.

Gautier, J.-M., E. H. Oelkers, and J. Schott (2001). Are quartz dissolution rates proportional to BET surface areas? *Geochimica et Cosmochimica Acta* 65 (7), pp. 1059–1070.

He, W, C Beyer, J. Fleckenstein, E Jang, O Kolditz, D Naumov, and T Kalbacher (2015). A parallelization scheme to simulate reactive transport in the subsurface environment with OGS#IPhreeqc 5.5.7-3.1.2. *Geoscientific Model Development* 8 (10), pp. 3333–3348.

Heidug, W. K. (1995). Intergranular solid-fluid phase transformations under stress: The effect of surface forces. *Journal of Geophysical Research: Solid Earth* 100 (B4), pp. 5931–5940.

Kolditz, O., S. Bauer, L. Bilke, N. Böttcher, J.-O. Delfs, T. Fischer, U. J. Görke, T. Kalbacher, G. Kosakowski, C. McDermott, et al. (2012). OpenGeoSys: an open-source initiative for numerical simulation of thermo-hydro-mechanical /chemical (THM/C) processes in porous media. *Environmental Earth Sciences* 67 (2), pp. 589–599.

Lang, P., A Paluszny, and R. Zimmerman (2015). Hydraulic sealing due to pressure solution contact zone growth in siliciclastic rock fractures. *Journal of Geophysical Research: Solid Earth* 120 (6), pp. 4080–4101.

Lange, R. A., H. M. Frey, and J. Hector (2009). A thermodynamic model for the plagioclase-liquid hygrometer/thermometer. *American Mineralogist* 94 (4), pp. 494–506.

Lehner, F. K. (1995). A model for intergranular pressure solution in open systems. *Tectonophysics* 245 (3), pp. 153–170.

Li, L., C. A. Peters, and M. A. Celia (2006). Upscaling geochemical reaction rates using pore-scale network modeling. *Advances in water resources* 29 (9), pp. 1351–1370.

Lu, R., N. Watanabe, W. He, E. Jang, H. Shao, O. Kolditz, and H. Shao (2017). Calibration of water–granite interaction with pressure solution in a flow-through fracture under confining pressure. *Environmental Earth Sciences* 76 (12), p. 417.

Lu, R., T. Nagel, H. Shao, O. Kolditz, and H. Shao (2018). Modelling of dissolution-induced permeability evolution of a granite fracture under crustal conditions. *Journal of Geophysical Research: Solid Earth*.

Luo, J., Y. Zhu, Q. Guo, L. Tan, Y. Zhuang, M. Liu, C. Zhang, W. Xiang, and J. Rohn (2017). Experimental investigation of the hydraulic and heat-transfer properties of artificially fractured granite. *Scientific reports* 7, p. 39882.

Lüttge, A., E. W. Bolton, and A. C. Lasaga (1999). An interferometric study of the dissolution kinetics of anorthite; the role of reactive surface area. *American Journal of Science* 299 (7-9), pp. 652–678.

Moore, D. E., D. A. Lockner, and J. D. Byerlee (1994). Reduction of permeability in granite at elevated temperatures. *Science* 265 (5178), pp. 1558–1561.

Neretnieks, I. (2014). Stress–mediated closing of fractures: Impact of matrix diffusion. *Journal of Geophysical Research: Solid Earth* 119 (5), pp. 4149–4163.

Ogata, S., H. Yasuhara, N. Kinoshita, D.-S. Cheon, and K. Kishida (2018). Modeling of coupled thermal-hydraulic-mechanical-chemical processes for predicting the evolution in permeability and reactive transport behavior within single rock fractures. *International Journal of Rock Mechanics and Mining Sciences*.

Palandri, J. L. and Y. K. Kharaka (2004). *A compilation of rate parameters of water-mineral interaction kinetics for application to geochemical modeling*. Tech. rep. Geological Survey Menlo Park CA.

Paterson, M. (1973). Nonhydrostatic thermodynamics and its geologic applications. *Reviews of Geophysics* 11 (2), pp. 355–389.

Polak, A, D Elsworth, H Yasuhara, A. Grader, and P. Halleck (2003). Permeability reduction of a natural fracture under net dissolution by hydrothermal fluids. *Geophysical Research Letters* 30 (20).

Polak, A., D. Elsworth, J. Liu, and A. S. Grader (2004). Spontaneous switching of permeability changes in a limestone fracture with net dissolution. *Water Resources Research* 40 (3).

Revil, A (1999). Pervasive pressure-solution transfer: A poro-visco-plastic model. *Geophysical Research Letters* 26 (2), pp. 255–258.

Rutter, E. (1983). Pressure solution in nature, theory and experiment. *Journal of the Geological Society* 140 (5), pp. 725–740.

Scheidegger, A. E. (1961). General theory of dispersion in porous media. *Journal of Geophysical Research* 66 (10), pp. 3273–3278.

Sidick, E. (2009). "Power spectral density specification and analysis of large optical surfaces". *Modeling Aspects in Optical Metrology II*. Vol. 7390. International Society for Optics and Photonics, p. 73900L.

Stebbins, J. F., I. S. Carmichael, and D. E. Weill (1983). The high temperature liquid and glass heat contents and the heats of fusion of diopside, albite, sanidine and nepheline. *American Mineralogist* 68 (7-8), pp. 717–730.

Stephenson, L., W. Plumley, and V. Palciauskas (1992). A model for sandstone compaction by grain interpenetration. *Journal of Sedimentary Research* 62 (1), pp. 11–22.

Tada, R. and R. Siever (1989). Pressure solution during diagenesis. *Annual Review of Earth and Planetary Sciences* 17 (1), pp. 89–118.

Taron, J. and D. Elsworth (2009). Thermal–hydrologic–mechanical–chemical processes in the evolution of engineered geothermal reservoirs. *International Journal of Rock Mechanics and Mining Sciences* 46 (5), pp. 855–864.

Taron, Joshua and Elsworth, Derek (2010). Constraints on compaction rate and equilibrium in the pressure solution creep of quartz aggregates and fractures: Controls of aqueous concentration. *Journal of Geophysical Research: Solid Earth* 115 (B7).

Tester, J. W., W. G. Worley, B. A. Robinson, C. O. Grigsby, and J. L. Feerer (1994). Correlating quartz dissolution kinetics in pure water from 25 to 625 C. *Geochimica et Cosmochimica Acta* 58 (11), pp. 2407–2420.

Walsh, J. (1981). "Effect of pore pressure and confining pressure on fracture permeability". *International Journal of Rock Mechanics and Mining Sciences & Geomechanics Abstracts*. Vol. 18. 5. Elsevier, pp. 429–435.

Weyl, P. K. (1959). Pressure solution and the force of crystallization: a phenomenological theory. *Journal of geophysical research* 64 (11), pp. 2001–2025.

Witherspoon, P. A., J. S. Wang, K Iwai, and J. E. Gale (1980). Validity of cubic law for fluid flow in a deformable rock fracture. *Water resources research* 16 (6), pp. 1016–1024.

Worley, W. G. (1994). "Dissolution kinetics and mechanisms in quartz-and grainite-water systems". PhD thesis. Massachusetts Institute of Technology.

Yasuhara, H., N. Kinoshita, H. Ohfuji, D. S. Lee, S. Nakashima, and K. Kishida (2011). Temporal alteration of fracture permeability in granite under hydrothermal conditions and its interpretation by coupled chemo-mechanical model. *Applied Geochemistry* 26 (12), pp. 2074–2088.

Yasuhara, H., A. Polak, Y. Mitani, A. S. Grader, P. M. Halleck, and D. Elsworth (2006). Evolution of fracture permeability through fluid–rock reaction under hydrothermal conditions. *Earth and Planetary Science Letters* 244 (1-2), pp. 186–200.

Yasuhara, Hideaki and Elsworth, Derek and Polak, Amir (2004). Evolution of permeability in a natural fracture: Significant role of pressure solution. *Journal of Geophysical Research: Solid Earth* 109 (B3).

Zhang, X. and C. J. Spiers (2005). Effects of phosphate ions on intergranular pressure solution in calcite: An experimental study. *Geochimica et Cosmochimica Acta* 69 (24), pp. 5681–5691.

Zhang, X., C. J. Spiers, and C. J. Peach (2010). Compaction creep of wet granular calcite by pressure solution at 28°C to 150°C. *Journal of Geophysical Research: Solid Earth* 115 (B9).

Zhu, C. and P. Lu (2009). Alkali feldspar dissolution and secondary mineral precipitation in batch systems: 3. Saturation states of product minerals and reaction paths. *Geochimica et Cosmochimica Acta* 73 (11), pp. 3171–3200.